J Mol Model (2005) 11: 210–225
DOI 10.1007/s00894-005-0255-8

ORIGINAL PAPER

Ileana Stoica

# Force field impact and spin-probe modeling in molecular dynamics simulations of spin-labeled T4 lysozyme

Received: 15 November 2004 / Accepted: 26 January 2005 / Published online: 2 April 2005


**Abstract** Several attempts have been made to compute electron paramagnetic resonance (EPR) spectra of biomolecules, using motional models or simulated trajectories to describe dynamics. Ideally, the simulated trajectories should capture "fast" (picosecond) snapshots of spin-probe rotations accurately, while being lengthy enough to ensure a proper Fourier integration of the time-domain signal. It is the interplay of the two criteria that poses computational challenges to the method. In this context, an analysis of the spin-probe and protein conformational sampling and equilibration, with different force fields and with explicit solvent, may be a useful attempt. The present work reports a comparative study of the effect of the molecular dynamics (MD) force field on conformational sampling and equilibration in two spin-labeled T4 lysozyme (T4L) variants, N40C and K48C. Ensembles of 10× 3 ns-trajectories per variant and per force field (OPLS/AMBER and AMBER99) are analyzed for a reliable assessment of convergence and sampling. It is found that subtle site-dependent differences in spin-probe rotations and torsions are more readily captured in the AMBER99 trajectories than in the OPLS/AMBER simulations. On the other hand, sampling and equilibration are found to be better with the OPLS/AMBER force field at equal trajectory lengths.

**Keywords** Molecular dynamics (MD) · T4 Lysozyme (T4L) · Force field · Electronic paramagnetic resonance (EPR)

I. Stoica
National Research Council of Canada,
Biotechnology Research Institute,
6100 Royalmount Avenue,
Montréal, QC, H4P 2R2, Canada
E-mail: istoica@physics.cornell.edu

## Introduction

Electron paramagnetic resonance (EPR) is a powerful experimental technique used to probe dynamics in proteins, membranes, and nucleic acids [1]. The shorter (compared to NMR) relaxation time of the excited electron enables the study of sub-nanosecond processes; in EPR, local spin-probe dynamics effectively modulates the electron spin Hamiltonian, making the technique more sensitive to local motions [1–5]. Essential advances of the technique (high-field EPR, multifrequency EPR [6]) allowed for the investigation of fast (sub-nanosecond) and localized (backbone and side-chain) fluctuations in spin-labeled proteins.

Considerable work has been devoted to developing a theoretical framework for the calculation of EPR lineshapes [7–11]. Some of the existing computational approaches, based on the Stochastic Liouville Equation, employ various models for the (classical) molecular motions of the spin probe and the protein backbone: rigid-body diffusion for the protein, combined with Brownian "diffusion in a cone" for the spin probe [7, 8], "two-site jumping" motion [11], Brownian dynamics (BD) [10–13], and finally, atomically detailed molecular dynamics (MD) [14].

Given their high (picosecond) time resolution and atomic detail, MD simulations can probe in exquisite detail local protein backbone and side-chain fluctuations, spin-label motions, as well as interactions between the labeled protein and the solvent. Thus, molecular dynamics provides an independent and complementary view on dynamics, which can be used within the Liouville Equation framework to simulate EPR spectra of biomolecules from first principles. MD simulations of spin-labeled lipids [14], of myosin [15], of photosynthetic units [16] and of spin-labeled T4L [17], have already been reported. The simulations were carried out with the purpose of extracting EPR-relevant information such as site-dependent spin-probe rotational diffusion constants and order parameters, but only a few [10, 14, 17] were

used to generate EPR spectra from atomically detailed trajectories.

The procedure faces computational challenges:

For the simulation of a proper EPR spectrum, the length of a trajectory must be of the order of the $T_2$ (transversal) relaxation time constant, i.e. of several 100 ns [10]. The need for trajectories longer than what was attainable with molecular dynamics on a spin-labeled lipid system [14] led to the extrapolation of the MD free induction decay by using a ''flexible BD model'', while in the study of T4, variants it was concluded that longer trajectories and more averaging over initial conditions were necessary for proper integration of the time-domain signal [17]. Often, the high mobility of the spin probe (partly dependent on the number of rotatable bonds that link the nitroxide probe to the adjacent cysteine side-chain [18]) results in motional averaging of the simulated spectra, which can be misleading when directly comparing simulations to experiment. Sometimes, the computational procedure itself is conducive to lower predicted order parameters [15], since calculations are based on the most populous mode in the spin-probe trajectory, many of which are at least bimodal.

In this context, it is important to examine the impact of the MD force field on spin probe (and protein) equilibration and local fluctuations, on order parameters and decay constants, and in capturing site-dependent motional features. The present analysis is based on ensembles of trajectories, thus offering a reliable (trajectory-averaged) assessment of equilibration and conformational sampling. As well, by considering two mutation sites with similar secondary structure and tertiary contacts, but with different degrees of local mobility [18]–N40 is a hinge residue [19]—it could be determined which of the force fields was more sensitive to site-dependent steric hindrances.

## Methods

### The proteins and the spin-label

Aspects of protein global and local dynamics are analyzed in a (MD) study of two spin-labeled variants of T4L (PDB entry: 114 L), previously used in ESR experiments [18]. The mutants, which will be referred to as N40C and K48C, are obtained experimentally by single-point mutations by which a cysteine residue is inserted, followed by attachment of the spin-probe via a disulfide bridge to the cysteine; the cysteine can be placed at various positions along the protein backbone [5, 18, 20, 21]. Experiments on more than 30 variants of T4L have been reported [5, 18, 21]. Also, doubly-labeled mutants have been prepared and studied in another series of (EPR) experiments [20] aimed at deriving structural information (distance constraints), as well as dynamic information on the lysozyme hinge-bending motion [20].

The spin-label molecule, which will be referred to as R1 [5, 10, 18, 20–22], is inserted at specific sites in the protein. The R1 has been used extensively in site-directed spin labeling (SDSL) in conjunction with EPR experiments [18, 20–22], and is a sulfhydryl-specific nitroxide reagent. To simplify the calculations, a ''reduced'' MTSSL molecule was used (see Ref. [23] for a similar choice), where the protective methyl substituents of the ring have been replaced with hydrogen atoms. A more in-depth discussion of this choice is presented in the Results section.

The pyrrole ring geometry was used as initial structure for R1. Three geometry optimization runs were then performed using GAUSSIAN (ROHF method, 6-31 + G** basis set). The partial charges on all ring atoms were computed using the restrained electrostatic potential (RESP) charge-fitting package from AMBER [24]. Since AMBER is an all-hydrogen force field, in the AMBER simulations all hydrogens in the R1 ring were included, with their computed partial charges, while for the OPLS/AMBER simulations an additional RESP fit was performed, with hydrogens summed up into the heavy atoms.

### The MD simulation protocol; force field implementation

The MOIL package [25] was used for the simulations described below. The force field in MOIL is OPLS/AMBER-based [26].

A second set of (MD) trajectories was produced using AMBER99, with the purpose of assessing the force field sensitivity to conformational sampling at the level of protein backbone, side-chain, and spin probe.

The implementation of AMBER99 in MOIL comprised reparametrizing atomic properties, as well as adapting the computation of some of the MOIL energy terms and non-bonded list criteria to the formulae used in AMBER. The new code was tested on small systems (ions, water boxes, alanine and valine dipeptide), large proteins (T4L [17]), and nucleic acids [27].

All simulations were performed in a periodic cubic box of size 60 Å filled with TIP3 water molecules. Crystallographic water molecules were also included, and chloride ions were added to ensure neutrality. A ''bad contact'' run was first performed, followed by minimization, heating to room temperature, and equilibration [17].

The use of SHAKE algorithm [28] to constrain bond lengths, and of MSHAKE for water molecules, allowed for a 2 fs-time step in the OPLS/AMBER simulations. Particle Meshed Ewald (PME) was used for long-range electrostatics [29], bond lengths were kept fixed, and protein translation was suppressed by adding a harmonic potential to the center of mass of the protein. Coordinates were saved every 0.2 ps. Velocities were initially sampled for each trajectory from a Maxwell distribution at 300 K, and were tested for rescaling (to fit room temperature) every 2 ps. In the AMBER

simulations, a smaller 1.5 fs time step was found optimal for convergence of SHAKE and MSHAKE, and coordinates were recorded every 0.15 ps. More details on the (MD) set-up are given elsewhere [17].

After 100 ps of equilibration at 300 K, a test run of another 1 ns was performed, at constant temperature (300 K). Along the dynamic trajectory, ten structures, equally spaced in time, were selected, and used as initial structures for the subsequent simulations. A total of ten trajectories per mutant per force field used were produced. The simulations were carried out on the group LINUX cluster and on a WINDOWS 2000 cluster, at Cornell Theory Center, in the Computational Biology Unit (CBSU). Approximately 4 months of computation time with each force field were necessary.

While the OPLS/AMBER trajectories were carried out to 5.5 ns and used further to compute EPR spectra [17], the AMBER trajectories were stopped at 3 ns and used as a force field sensitivity check only. However, in the present work, which is a comparison study, all analyses were carried out on 3 ns-trajectories, i.e. the final 2.5 ns pieces of the OPLS/AMBER trajectories were not used. To capture the conformational spread during MD visually, in Fig. 1 we present sample lysozyme structures at the start of one dynamic trajectory and after completion of the simulation, respectively.

## Analysis of global and local motions

For analyzing global and local motions (at the level of protein backbone, side-chains, or spin probe), the Kabsch rotation matrix procedure [30, 31] was used. The rotation matrix $U$ best overlaps a given coordinate set to the initial (reference) coordinates (e.g. the $C_\alpha$-trace for global motion analysis), at each time point along the dynamic trajectory. The rotation matrix defines a system rotation axis, as well as the angular degrees of freedom: the angle $\Omega$ of rotation about the axis, and the polar angles $\theta$ and $\Phi$ which define the position of the axis vector in the absolute (reference) frame.

Local motions need to be treated in a reference frame corrected for overall protein rotation. For this purpose, a $U^{-1}$ transformation was first applied to the MD trajectory, after which rotational degrees of freedom were computed for a selected set of atoms (e.g. the spin probe). An illustration of the spin-probe degrees of freedom that the present study will focus on is given in Fig. 2.

Autocorrelation functions of the spin-probe rotational degrees of freedom were computed with a sliding time window:

$$\mathrm{Corr\_cos}(\tau) = 1n\langle \cos\,\Phi(t)\cos\,\Phi(t+\tau)\rangle_{t=n\Delta t}. \tag{1}$$

For variations in rotation angles, a sine-correlation function was calculated, thus eliminating constant terms from the Taylor expansion:

$$\mathrm{Corr\_sin}(\tau) = \frac{1}{n}\langle \sin\,\Delta\Phi(t)\sin\,\Delta\Phi(t+\tau)\rangle_{t=n\Delta t}. \tag{2}$$

The second-moment correlation function (zero-order) was defined as [14]:

$$C_0(t) = \langle P_2(\cos(\theta(t)-\theta(t_0))\rangle_{t_0} = \left\langle D^{2*}_{00}(\theta(t))D^{2}_{00}(\theta(t_0))\right\rangle_{t_0} \tag{3}$$

and was computed for the $\theta$-angle between the normal to the ring plane and the laboratory $z$-direction (magnetic field). $D^2_{00}$ are second-rank Wigner matrices:

$$D^2_{00} = \frac{3\,\cos^2(\theta-1)}{2}. \tag{4}$$

The correlation decay time $\tau$ was defined as:

$$\tau = \int_0^\infty \frac{C_0(t)}{C_0(0)}\mathrm{d}t. \tag{5}$$

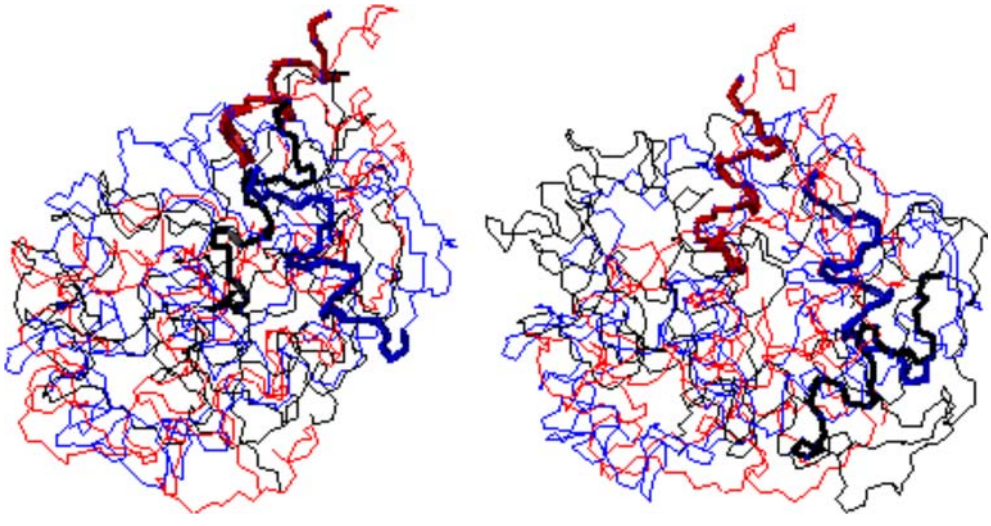

**Fig. 1** Three selected structures (*number* 1, 4 and, 7) of the N40C AMBER ensemble: snaphots at time 0 (*left*) and 3 ns (*right*); helix B *highlighted*. Figure generated with MOLMOL [34]

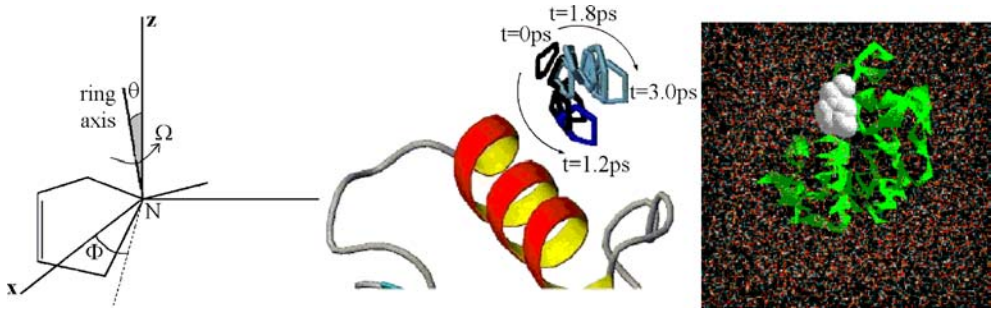


**Fig. 2** *Left panel* the spin-probe R1 ring and the spin-probe Euler angles Ω, $\theta$ and Φ. *Middle panel* illustration of the "diffusion in a cone" model for the spin-probe motion: snapshots of helix B and of the R1 ring in N40C, taken at 0.3 ps intervals from AMBER trajectory 1, corrected for all-protein motion; figure generated with MOLMOL [34]. *Right panel* the N40C mutant with the spin label (*solid mode*), solvated in a cubic box; figure generated with the MOIL graphical interface [25]

## Results and discussion

### Analysis of global motions

Analysis of atom-positional root mean square deviations (RMSD) values provides a quality check of the simulations, as well as a criterion for convergence [32].

As shown if Fig. 3, at corresponding simulation times (RMSD) from the starting structures were found to stabilize after around 1ns, in both the OPLS/AMBER and the AMBER trajectories. $C_\alpha$ RMSD values were smaller in the AMBER trajectories at comparative time points, which indicates smaller backbone fluctuations in the AMBER trajectories. However, the all-protein rotational diffusion in solution (measured by the protein tilt angle $\theta_{\text{prot}}$, as computed from the rotation matrix $U$) seemed to cover a comparable or larger range than in the OPLS-trajectories, as can be seen in Fig. 4.

With both force fields, the starting structures for the ten trajectories were extracted from an initial single 1 ns MD trajectory, by saving coordinates at 100 ps intervals. Therefore, the conformations were increasingly farther away on the energy landscape from the original minimized starting structure (see Ref. [15] for a similar choice). The trajectories uniformly converged after roughly 1 ns, which eliminates the possibility of convergence sensitivity to initial conformations, as long as the starting RMSD (to the minimized structure) was not higher than ~1 A.

### Analysis of spin-probe rotations

#### *The bimodal exchange model of MTSSL motion*

A key step in the EPR line-shape interpretation is identifying the rotational and torsional restrictions at the attachment site, and correlating them with the presence of immobilized components in the spectrum [5, 6, 10, 18, 21, 22].

On the basis of EPR spectral analysis, the two T4L mutants have been placed in the category of solvent-exposed, fairly mobile sites on the surface of α-helices [18]. The crystallographic and MD-computed *B*-factors indicate high-amplitude thermal fluctuations at both labeling sites [17].

Another fundamental feature that characterizes the nitroxide attached to a protein is its solvent accessibility [18]. The two labeling sites have high solvent-accessibility areas, slightly higher in the case of N40 [19]. Water molecules in the proximity of the MTSSL ring (N–O bond) were typically found to have high-diffusion rates and short residence times, with some interesting exceptions in the case of K48C [19].

To capture aspects of spin-probe motion better, we examined the probability densities in the probe rotational space. The trajectory-averaged distribution functions reveal the number of orientational states and the extent of disorder about each configuration [15].

The ring rotational and side-chain torsional motions were analyzed in a frame corrected for protein rotations, as described in the Methods section. At each time point, triplets (Ω, $\theta$, Φ)($t$) were extracted from the rotation matrix $U(t)$. 2-Dimensional probability density plots were calculated from Euler angle populations [17]. The projection was done on the ($\theta$, Φ) axes, and normalization was done with respect to the total number of sampled points, and to the size of the bins (60 slices were considered, meaning a 3°—box for the $\theta$ sampling, and 6° for the Φ sampling). An average over eight trajectories (excluding the two extremes in backbone RMSD) was performed for the graphs in Fig. 5.

The "bimodal exchange" profile of the Euler angle probability density indicates the existence of two preferred spin-probe discrete orientations, with transitions between them occurring in a "jump" diffusive-like manner on the nanosecond time scale [10], in agreement with existing models [10, 11, 21].

The existence of multiple peaks in the AMBER two-dimensional sampling probabilities (Fig. 6) is most probably due to insufficient sampling and averaging, as well as to more frequent sampling and saving of atomic coordinates. In contrast to the OPLS/AMBER simulations, equilibration in the spin-probe rotations could not be achieved on the nanosecond time-scale (more on this later).

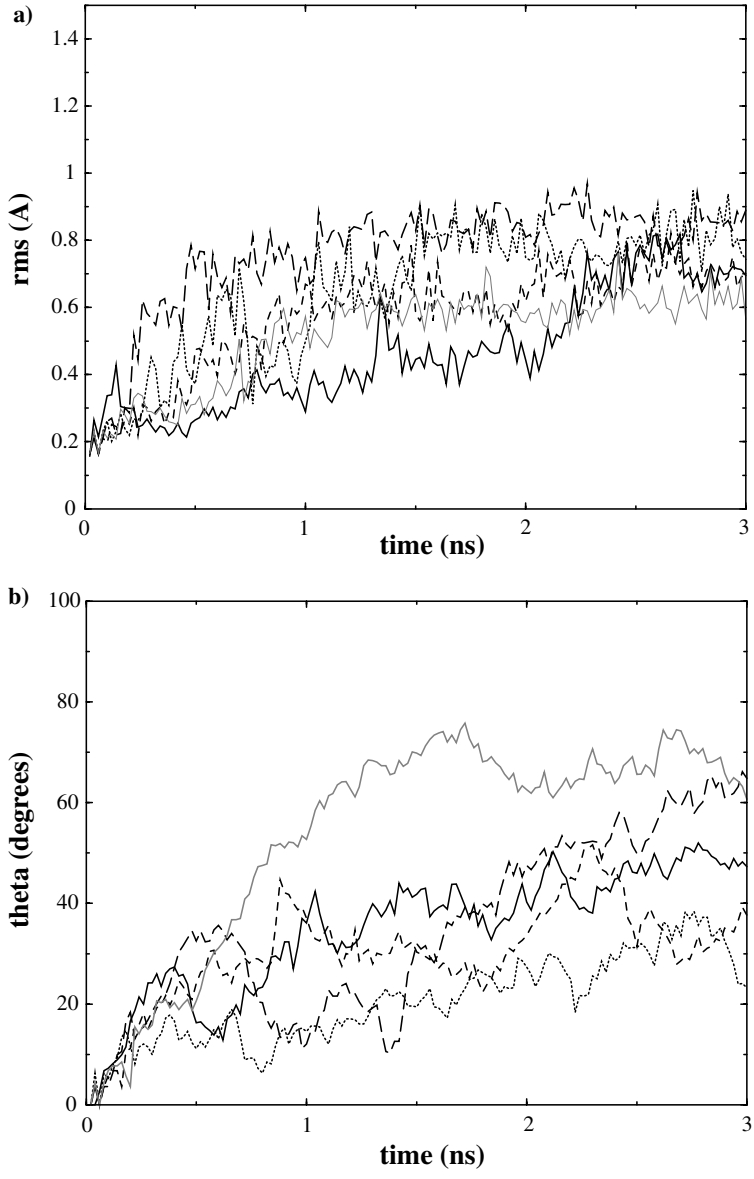


**Fig. 3** $C_\alpha$-RMSD values (a) and all-protein tilt angle (b) in five selected K48C AMBER99 trajectories

*Extension of trajectory time; force field considerations*

Adequate sampling of the spin-probe rotational degrees of freedom and equilibration of spin-probe motion during the simulation time are implicit requirements to compute sampling probability densities correctly and to use them further in simulating EPR spectra. Therefore, it is necessary to assess equilibration and convergence on the trajectory time scale of a few nanoseconds, as well as to compute the relevant time constants for the inertial/diffusive motion of the spin label in the Euler angle space. As well, it is worthwhile to understand the effect of force field on all the above computations.

Examining the extent of equilibration and conformational sampling is also important from a more technical point of view. Given the necessity for long (hundreds of nanoseconds) spin-probe trajectories, procedures can be devised to "append" individual trajectories into a unique extended trajectory [17]. For this procedure to be meaningful, there should not exist conformational "jumps" at the points of appendage, i.e.

(1) equilibration should have been achieved within one individual trajectory and
(2) sampling should be independent of the starting configuration (within one trajectory time, the region of the rotational space sampled should not be confined around the starting point). We tested these assumptions with both force fields, and found that they hold only in the OPLS/AMBER case. We are presenting two alternative procedure checks:

(1) We used the quantity

$$\gamma_{\delta t}(t) = \frac{\mathrm{Tr}\{U(t)U^T(t+\delta t\}}{3} \tag{6}$$

which is the trace of a product of rotation matrices, normalized to the trace of the identity matrix, in

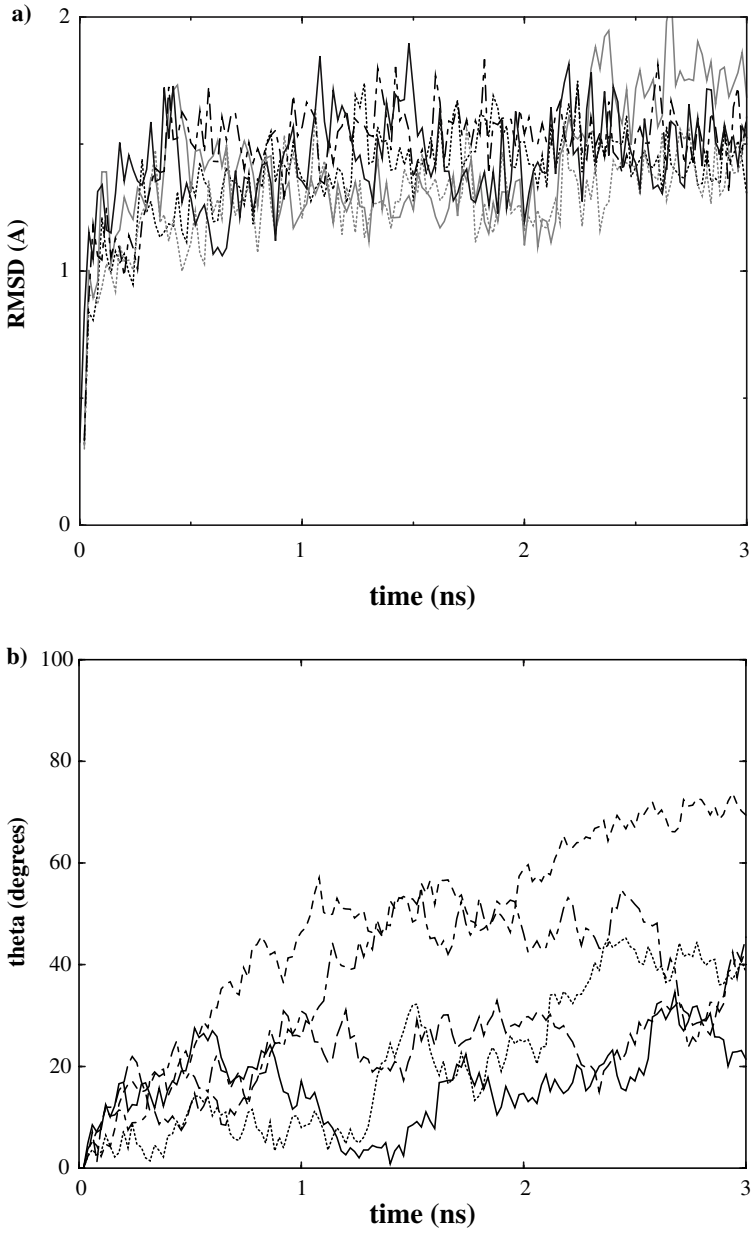


**Fig. 4** $C_\alpha$-RMSD values (a) and all-protein tilt angle (b) in five selected K48C OPLS/AMBER trajectories

order to quantify the Euler angle variations (essentially $\delta\Omega$) within the time interval $\delta t = 0.2$ ps used for recording spin-probe coordinates. For Fig. 7a 2×10×3 ns = 60 ns trajectory was used, obtained by appending the ten individual trajectories, first in the order 1–10, and then reversed (10 to 1). A 20 ns-strip of the $\gamma$-trace around the mid point is presented, to illustrate the absence of high "jumps" around points of appendage.

(2) We compared the trajectory-averaged rotational probability densities presented in Fig. 5 to the probability densities calculated on an "appended" trajectory, where normalization is done with respect to the total number of points. 7×3 ns trajectories and a 21 ns-trajectory, respectively, were used for the analysis presented in Fig. 8.

By confirming the achievement of equilibration and the independence of conformational sampling on the initial configuration during each single trajectory, the tests above allowed for the extension of the total time scale, which is essential in EPR line-shape simulations [17]. These "appended" trajectories, while smaller than those attainable with BD simulations [10, 11, 12, 13, 14], are comparatively longer than other spin-probe MD trajectories [15] and benefit from the additional advantage of incorporating solvent effects explicitly.

The above equilibration and sampling patterns were not reproduced in the AMBER simulations, indicating that on the time scale of individual 3 ns-trajectories, full exchange between high-density states in the Euler angle space was not achieved, hence the persistence of a slower-decaying mode in autocorrelation functions (see below).

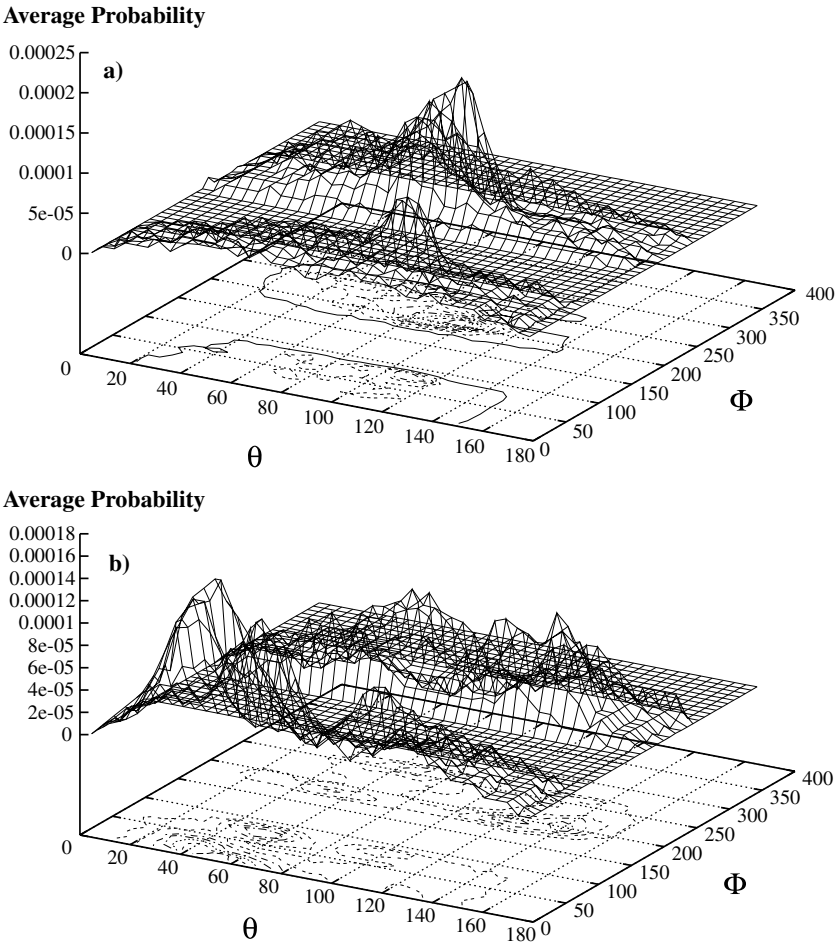


**Fig. 5** 2D-sampling probability density of $P(\theta, \Phi)$; average over 8 3 ns-OPLS/AMBER trajectories of N40C **(a)** and K48C **(b)**

*Effect of motional model and spin-probe modeling on rotational correlation times*

The interpretation of EPR line-shapes in terms of local structure and dynamical properties, on the one hand, and the reverse problem, the prediction of EPR line-shapes from first principles, on the other hand, critically depend on two factors: [18] the structure of the nitroxide itself, and the motional model used.

In the following paragraphs we present a combined analysis of both factors:

In MD simulations it is possible to examine motions with sub-picosecond time resolution and in atomic detail. In a small molecule reference frame, the spin-probe degrees of freedom are the Euler angles $\Omega$, $\theta$ and $\Phi$, to which the side-chain torsional angles $\chi$ should be added. Autocorrelations of the above angles are used to extract relevant time scales and motional features.

The analysis of Euler-angle autocorrelations shows that the variations $\Delta\,\Omega$, $\Delta\,\theta$ and $\Delta\,\Phi$ appear to be highly uncorrelated, which is an indication of the randomness of the nitroxide motion on the sub-picosecond time scale (Figs.9, 10).

The absence of angular velocity correlations suggests that the more widely used modeling of the spin-label motion as Brownian diffusion in an orienting potential [8, 10, 11, 18, 21] is a good approximation. Simulating the MTSSL as a particle diffusing in a potential of mean force and subject to the Langevin equation of motion benefits from a considerably smaller number of degrees of freedom, as well as from the possibility of extending the trajectory to more biophysically (and spectroscopically) meaningful time scales. In fact, it has often been suggested [10, 14, 15] that MD should be used to compute an effective potential of mean force accurately, on the basis of which the trajectory can be extended further with stochastic dynamics. A problem with this is the need to enhance conformational sampling so as to cover a larger configuration space than is available at room temperature, hence the high-temperature simulations [10, 15].

A common trend, apparent in previous studies [10, 15] as well as in the present autocorrelation profiles, was that the spin-label exhibited a "fast" or "inertial" motional mode (tens of picoseconds) and a "slow" or "diffusive" mode (hundreds of picoseconds to nanoseconds).

The inertial motional regime describes motion with little friction and dominated by the potential energy gradients, therefore well approximated by Newtonian mechanics. In fact, the inertial correlation times for all

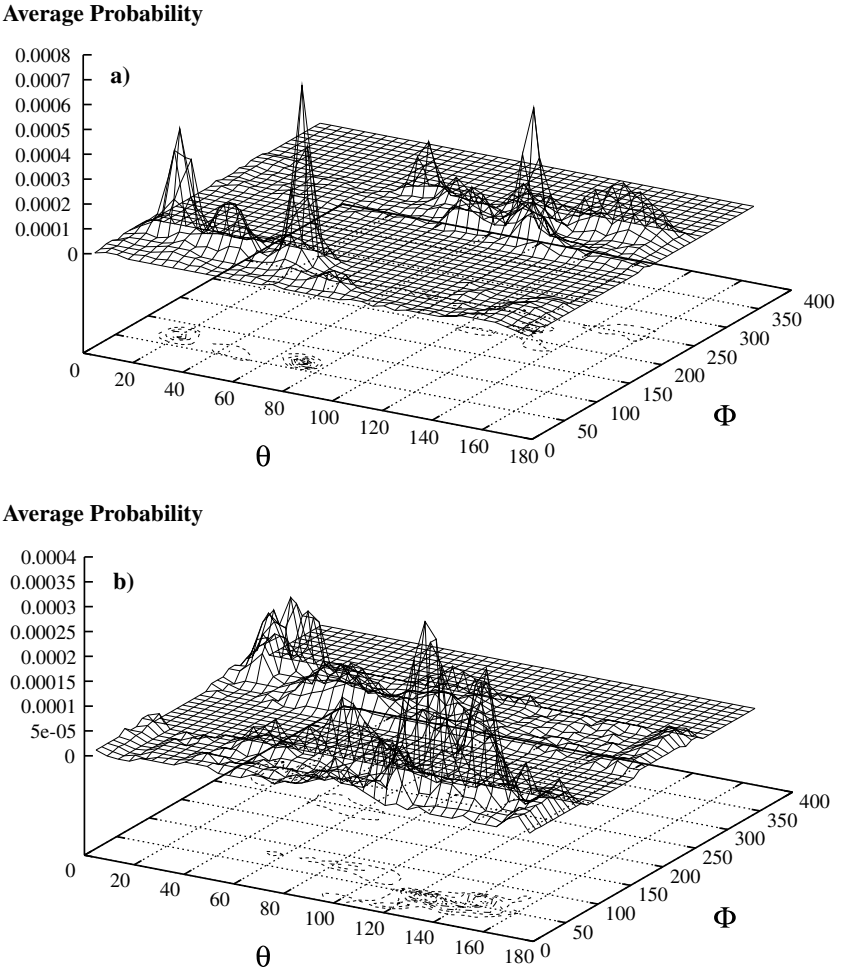


**Fig. 6** 2D-sampling probability density of $P(\theta, \Phi)$; average over 8 3 ns-AMBER trajectories of N40C (**a)** and K48C (**b)**

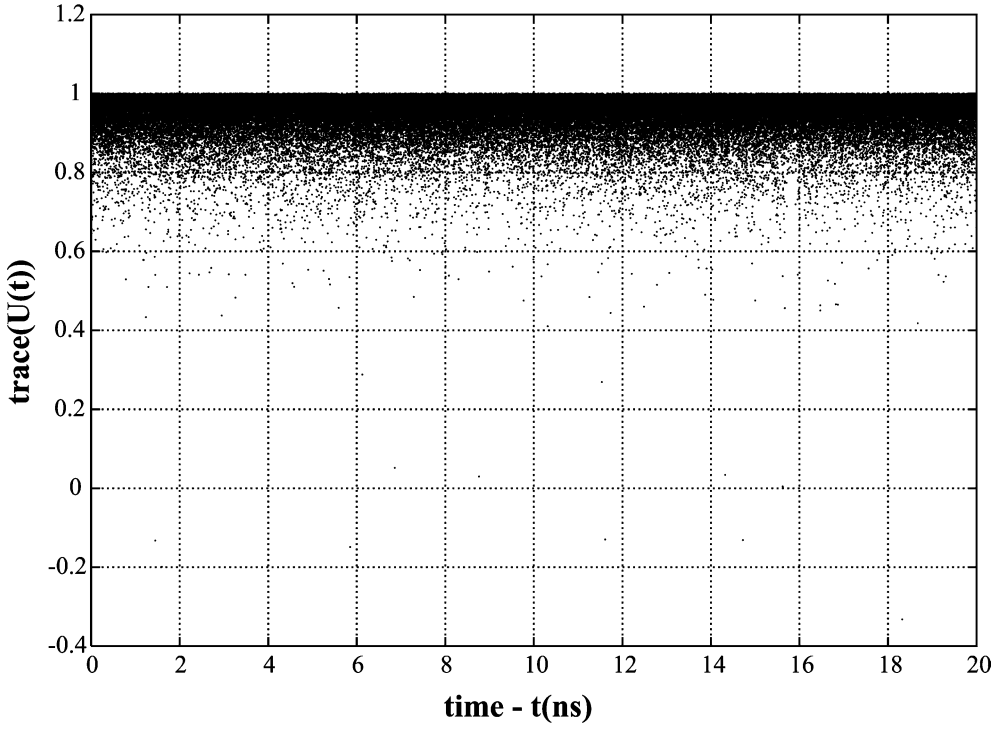


**Fig. 7** $\gamma(t)$—plot for the rotation matrix "jumps" along a 20 ns-portion of the overall "appended" 60 ns OPLS/AMBER trajectory of N40C. The 20 ns-strip was extracted around the appendage point of the first and second 30 ns-pieces of trajectory

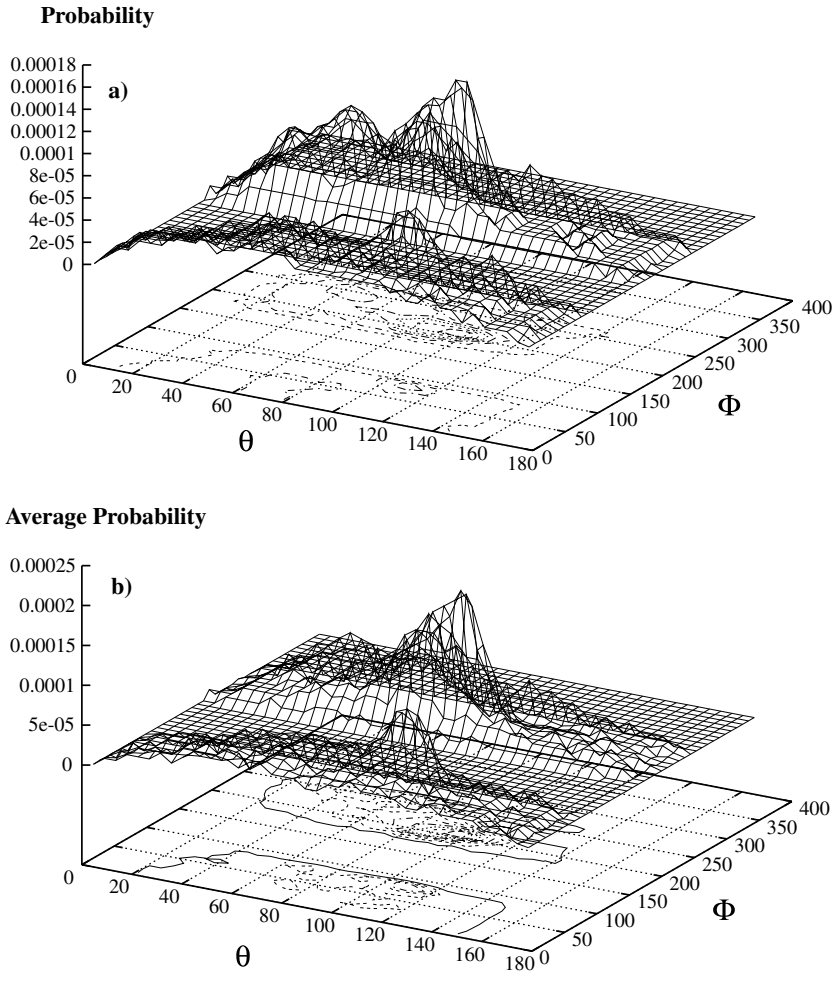


**Fig. 8** N40C—2D probability density $P(\theta, \Phi)$; average over an "appended" 21 ns-trajectory **(a)**, and over the seven individual 3 ns OPLS/AMBER trajectories **(b)**

rotational and torsional degrees of freedom (between 13.5 and 28.1 ps) are of the order of $\tau_{free}$, of a freely rotating particle, as reported in the study of Steinhoff and Hubbell (6 ps with a friction constant of 4 $ps^{-1}$ [10]), or as measured experimentally for free nitroxide rings diffusing in aqueous solutions (17 ps [33]).

While the inertial limit captures the oscillations of the MTSSL within local minima, the diffusive regime describes the transitions between such potential minima, occurring in our OPLS/AMBER trajectories on time scales from 0.1 to 3 ns. This time scale is, again, consistent with other studies (Steinhoff and Hubbell ascribe to the diffusive rotational correlation time a value above 500 ps [10]).

From a 14 ns MD trajectory of FDNASL attached to myosin, LeConte et al. identify three types of motion: a "very fast" ($<1$ ps) decay caused by spin-label atoms moving at room temperature, a "fast" ($\sim$50 ps) exploration of a given dynamics mode, and a "slow" component due to transitions between modes (500 ps but possibly up to several nanoseconds [15]). Furthermore, based on the estimate of viscous effects given by Steinhoff and Hubbell [10], they infer that the above rotational correlation times could increase by a factor of three if solvent is to be accounted for [15].

The pioneering simulations reported by Steinhoff and Hubbell were carried out on simplified models (MTSSL attached to a single cysteine or to a polyleucine trimer) and under simplifying assumptions (no solvent, and no Coulomb interactions). The MD calculations of LeConte et al. were also performed in vacuo, and on a subset of allowed motion, defined to consist of all atoms within 20 Å from the nitroxide N in FDNASL [15].

Compared to previous studies of spin-labeled peptides or proteins, our simulations have the advantage of atomic detail and explicit incorporation of solvent molecules, but suffer from the omission of the methyl groups, which decrease the bulkiness, hydrophobicity and inertial moment of R1, as well as affect the steric hindrance for side-chain torsions. In the following we give a brief estimate of the impact of our R1 model on the results presented in this manuscript.

We believe that the "very fast" decay observed by LeConte et al. is filtered out in our simulations for two reasons:

(1) The coordinates of the N–O bond, (which define the Euler angles) are saved in Ref. [15] every step (3 fs), while in our simulations (OPLS/AMBER) they are propagated every 2 fs, but recorded every

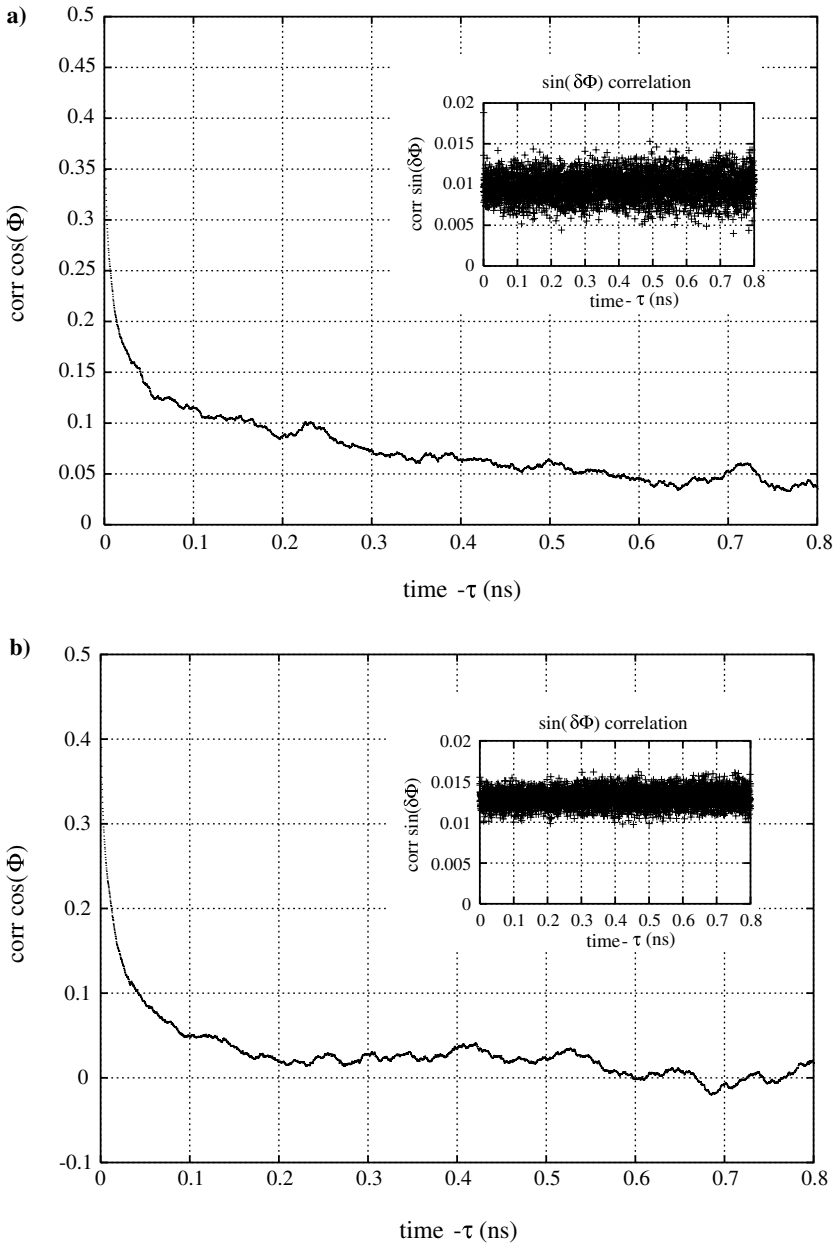


**Fig. 9** Autocorrelation functions for the Φ -angle and for variations of Φ within one time step (0.2 ps); average over 8 3 ns-trajectories of N40C **(a)** and K48C **(b)**; OPLS/AMBER trajectories

0.2 ps, which leads to some averaging of very fast modes.

(2) The ring and N–O bond being fairly rigid, the most likely contributors to $<1$ ps rotations are the protective methyl groups, which are not present in our reduced R1.

The absence of a very fast component makes it easier for us to identify and fit the other two. Our "fast" correlation times are smaller than those reported in Ref. [15] and closer to the freely diffusing nitroxide in Ref. [10] because the R1 probe is smaller than FDNASL and less sterically restricted (partially because of its reduced geometry, but also because of the high thermal factors and solvent exposure at the attachment sites).

However, we still have to account for the underprediction of correlation times caused by the omission of the four methyl groups:

A simple (and rough) geometrical calculation shows that the moment of inertia $I_{zz}$ about the ring axis increases by a factor of three upon inclusion of methyl groups, $I_{xx}$ about the in-plane axis parallel with the N–O bond increases by a factor of 5, and $I_{yy}$ (perpendicular to the NO bond) by 1.15.

In the inertial regime (small frictional forces), the Langevin equation in rotational space is dominated by the last two right-hand side terms:

$$I_i \frac{\mathrm{d}\omega_i(t)}{\mathrm{d}t} = -I_i f \omega_i(t) - \frac{\partial U_{\mathrm{eff}}(X)}{\partial X_i} + R_i(t) \tag{7}$$

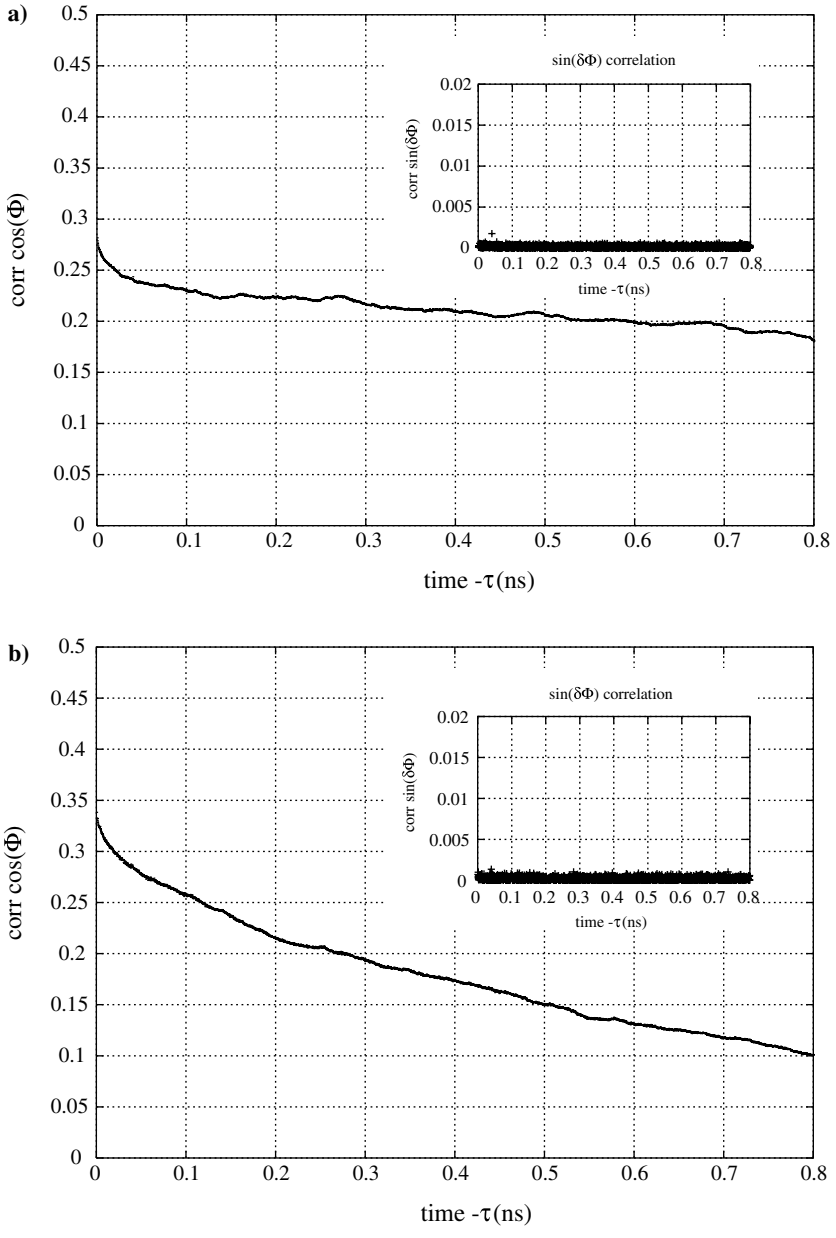


**Fig. 10** Autocorrelation functions for the Φ -angle and for variations of Φ within one time step (0.15 ps); average over 8 3 ns-trajectories of N40C **(a)** and K48C **(b)**; AMBER trajectories

In the above formula, $i$ denotes: $xx$, $yy$ or $zz$ as described previously, $\partial U_{\mathrm{eff}}(X)/\partial X_{\mathrm{i}}$ is the derivative of the potential of mean force at configuration $X$ with respect to the rotational parameter $X_{\mathrm{i}}$, (which can be $\Omega$, $\theta$ or $\Phi$), and $R(t)$ is the random force described by a Gaussian distribution of zero mean and satisfying the fluctuation-dissipation relation [10]. In the inertial regime $\mathrm{d}\omega_{\mathrm{i}}(t)/\mathrm{d}t$ will be proportional to $1/I_{\mathrm{i}}$, in other words the motion around the $z$-axis (in-plane $\Omega$ -rotation) slows down by a factor of 3 and with it the correlation time $\tau_{\Omega}$ increases threefold, $\tau_{\theta}$ ($x$-rotational correlation time) is underpredicted by a factor of 5, while $\tau_{\Phi}$ remains practically unchanged. These factors will push the inertial correlation times into the 50 ps range, with solvent effects inherently included.

In the diffusive regime, the frictional term (first right-hand side term in Eq.7) dominates, therefore both left-hand and right-hand side terms are proportional to the moment of inertia $I$. This shows the independence of the equation of motion, in this particular limit, on the inertial properties of the particle. Thus, we do not believe that the slow dynamics of the spin-label will be dramatically altered by its increased moment of inertia. Or, in the simulation of EPR line-shapes, it is the long-time behavior of the MTSSL (the slow, diffusive component), which determines whether or not the EPR tensors will be motionally averaged [15].

Finally, the simplest view is that of an isotropically diffusing particle. At a given temperature and friction constant, rotational diffusion correlation times scale with the volume of the particle according to Debye's law: $\tau_{\mathrm{c}} \sim \eta\, V/k\mathrm{T}$. Assuming a geometry-based $< 4$ times increase in the volume upon adding of the methyl groups, the correlation times obtained with a "true" R1

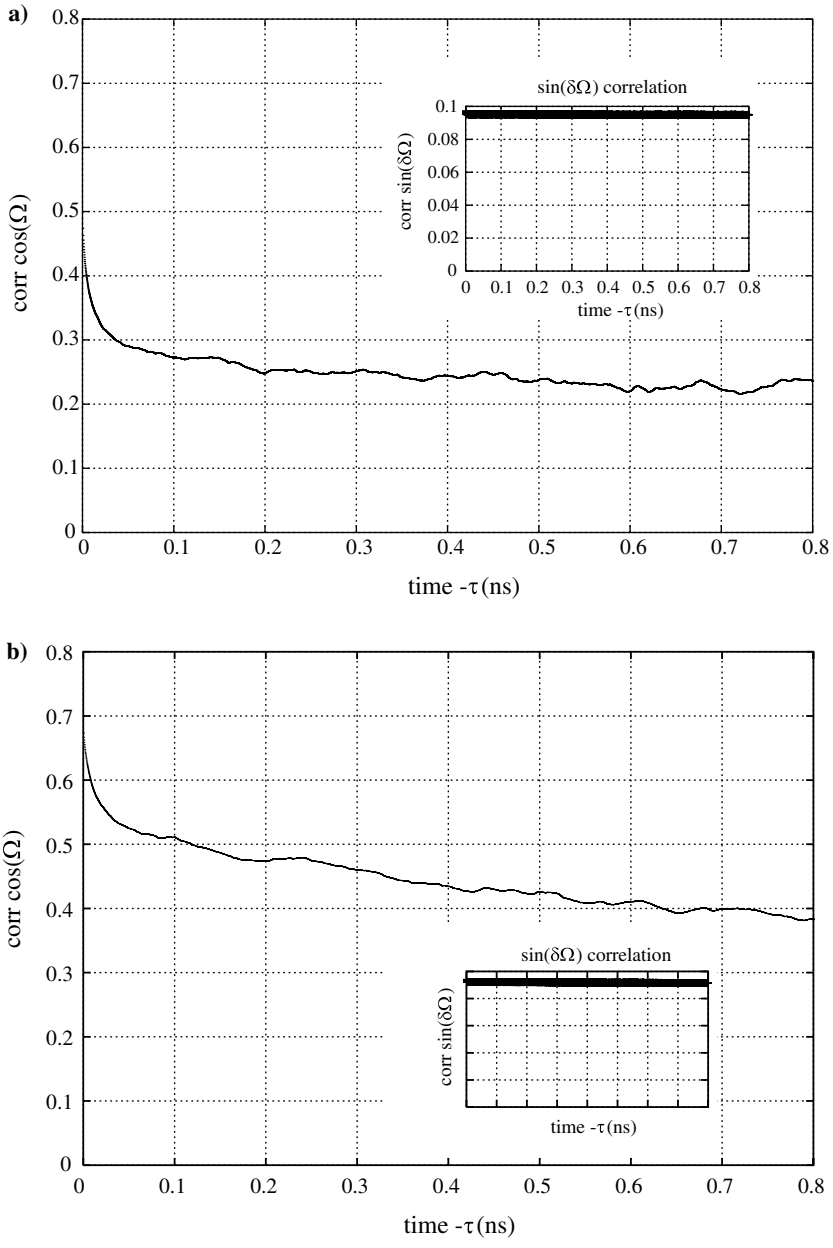


**Fig. 11** Autocorrelation functions for the Ω -angle and for variations of Ω within one time step (0.2 ps); average over 8 3 ns-trajectories of N40C **(a)** and K48C (**b**); OPLS/AMBER trajectories

model will scale up fourfold. A similar ratio (of 3) is given in Refs. [10, 15] to correct for the absence of solvent interactions and viscous drag.

These corrections do not alter significantly the overall characteristics of spin probe motion: randomness in angular velocity sampling, bimodal exchange profile of probability densities, ~3 orders of magnitude between the inertial and diffusive time constants, and motional averaging on the >100 ns time scale. In addition, the sites chosen for modeling in the present study do not exhibit strong tertiary interactions, and fall into the category of loosely ordered sites [18]. Thus, the removal of methyl groups and with it of some interactions with neighboring side-chains is not likely to alter key features in the probe rotations.

In fact, LeConte et al. [15] raise the very important question of using local protein topology (interactions, steric hindrances) as a predictor of mobility and spin-probe dynamic properties. They conclude that side-chain interactions with the spin label, the chemical nature of neighboring residues, and packing densities of protein atoms within a 5 Å sphere around the spin probe did not correlate with the actual nitroxide order parameter, suggesting that "spin-probe dynamics is a

more complicated story'' [15]. Also, in the comprehensive study of Mchaourab et al. [18], the analysis of nitroxide side-chain motions at the surfaces of α-helices, without tertiary interactions and with high solvent accessibility, led to the conclusion that the main determinant of the side-chain motion are not interactions with the nearest neighbors within the helix, but rather the dynamics of the protein backbone.

*Effect of force-field parametrization on correlation times*

An incomplete decay of the trajectory-averaged autocorrelation function was apparent in the AMBER force-field trajectories (Fig. 10). The reason is that on the time scale of the AMBER trajectory (3 ns), full exchange between high-density states in the Euler angle space was not achieved, hence the persistence of a slower-decaying mode.

The relevant rotational degrees of freedom, which modulate the spin Hamiltonian via the second order Wigner matrix elements and thus make the connection between the spin-probe molecular motion and the spin energies, are only $\theta$ and $\Phi$. However, an analysis of $\Omega$ -rotations about the spin-probe axis is necessary for the completeness of the force-field comparison.

In fact, sampling of the $\Omega$ angle appeared to be most dependent on the force field, and also to differentiate most between the motional characteristics of the two lysozyme variants.

In the OPLS/AMBER trajectory-averaged $\Omega$ -correlation, decay to a constant threshold was achieved for both T4L variants (Fig. 11). Again, there was a small

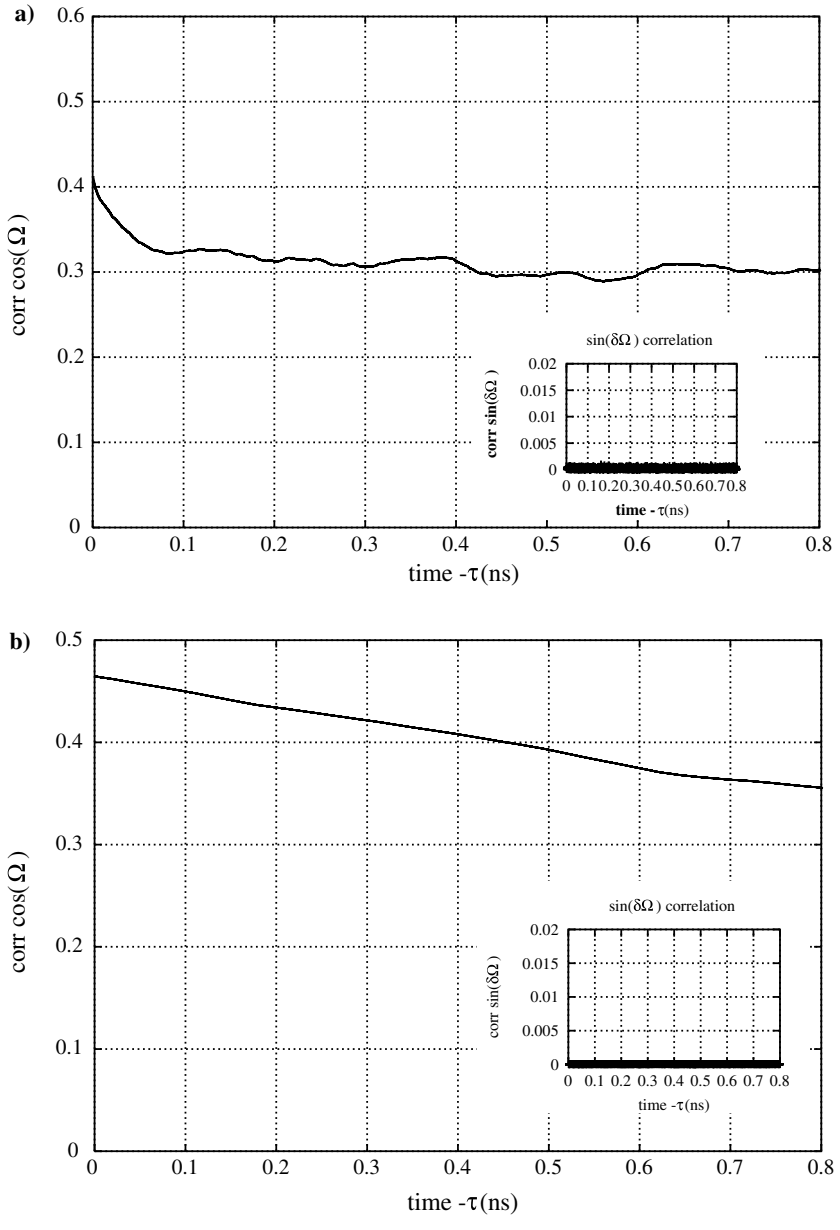


**Fig. 12** Autocorrelation functions for the Ω -angle and for variations of Ω within one time step (0.15 ps); average over 8 3 ns-trajectories of N40C **(a)** and K48C **(b)**; AMBER trajectories

residual $\Delta\Omega$, which suggested slight deviations from a perfect Brownian rotational diffusion in the OPLS/AMBER trajectories.

In the AMBER force-field simulations more pronounced distinctions between the two mutants were apparent in the 3D-sampling and 2D-sampling probability profiles (results not shown [17]). Most of these differences rose from sampling of the $\Omega$ -angle (Fig. 12). In N40C, motions about the rotation axis appeared to decay faster; full decay of the trajectory-averaged autocorrelation function was not achieved on the time scale of the simulation; however, in N40C, within half a nanosecond, a plateau was reached, which indicated the existence of a steric hindrance in motions about the ring axis. In K48C, the autocorrelation function did not decay to a constant value in 1 ns.

These results suggest that $\Omega$ -motions about the probe $z$-axis are more restricted than librational ($\theta$, $\Phi$)-motions about the nitroxide's $x$ and $y$ axes.

In addition, in-plane $\Omega$ rotations are more restricted in the AMBER simulations than in the AMBER/OPLS trajectories. The results also indicate that the AMBER force field simulations capture the differences in $\Omega$ (in-plane) rotation between the spin-labeled variants better: N40C exhibits a higher degree of rotational mobility, which may be due to its identification as a "hinge" residue [19]. The analysis of second-moment correlations (computed as described in the Methods section) confirmed that equilibration was incomplete in the AMBER trajectories: trajectory-averaged second moment correlations did not decay in the AMBER simulations (result not shown).

Identifying force fields that capture fast (picosecond) details of spin-probe motion, while avoiding "partial blurring" of distinct modes in the spectrum due to fast exchanges between rotameric states [10], is a challenging task. In addition to the force field choice, adequately tuning the interplay between the time step used by the MD propagator and the total time of a trajectory, as well as averaging over many more initial conditions, are necessary. Because of computational challenges, alternative methods are often implemented, either to extend the total length of a trajectory or to generate an ensemble of starting conditions [10, 15, 17].

## Torsional degrees of freedom

Torsion angles (numbered $\chi_1$ to $\chi_5$ as going from the protein backbone towards the spin-probe ring) can be computed as a function of time, as shown in Fig. 13.

The analysis of torsion angle fluctuations suggests the same multi-modal pattern, with rare (nanosecond scale) "jumps" between discrete rotameric states.

In each of the mutants and with both force fields, the torsional mobility was quantified by the average number of flips between the rotameric states in 3 ns. Trajectory-averaged numbers of $\chi$-transitions were similar in the OPLS/AMBER and AMBER trajectories, for both mutants, and slightly higher in the AMBER trajectories (result not shown). An analysis described elsewhere [17] suggested that in the OPLS/AMBER simulations the $\chi_1$ and $\chi_2$ populations were similar for N40C and K48C. The same result was obtained from the AMBER simulations (result not shown). In the same analysis, it was also observed that torsion angle fluctuations were essentially uncorrelated with spin-probe rotations [17].

No substantial difference in the autocorrelation decay times of $\chi_4$ and $\chi_5$ could be observed in the two mutants (Fig. 14): the short (inertial) time constant was not larger than 20 ps, while the long (diffusive) decay time was

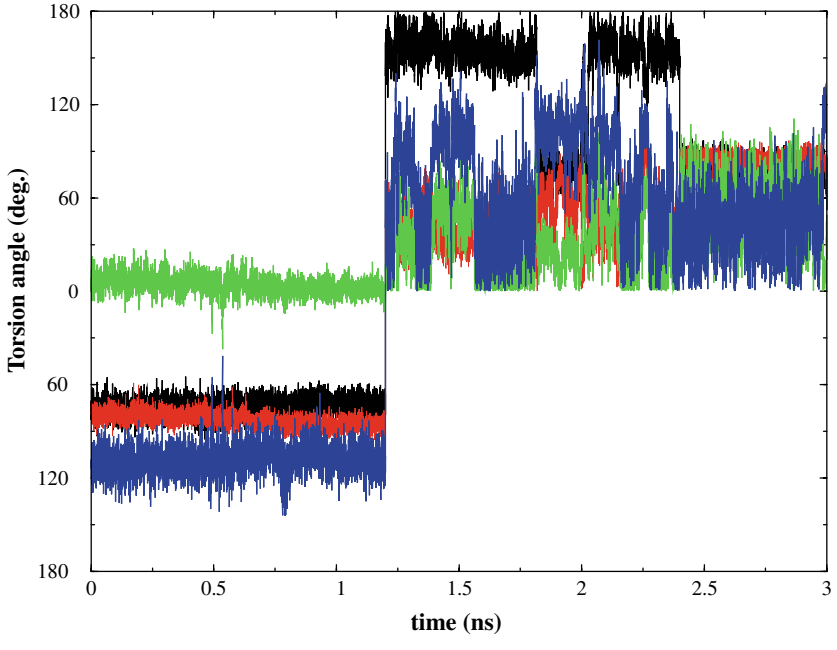


**Fig. 13** R1—CYS torsion angle fluctuations in 3 ns of motion of K48C; AMBER trajectory 4; *black* $\chi_2$, *red* $\chi_3$, *green* $\chi_4$, *blue* $\chi_5$

between 200 and 500 ps. In the AMBER simulations, the "slow" correlation times were pushed closer to 1 ns, which confirms the persistence of a slower-decaying mode and failure to achieve equilibration.

Overall, our conclusion was that the R1 model used in the present work was fairly insensitive to cysteine side-chain and protein-backbone fluctuations. This may be due to the large number of intermediate rotatable bonds in R1 [18]. The absence of the methyl substituents in our reduced R1 model is likely to have led to less steric hindrance of side-chain torsions and by doing this it could have obscured the site-dependent differences between the two proteins. The effect would have been more substantial in highly ordered virtual mutants, with significant tertiary contacts and little solvent exposure. However, we do capture the multi-component motional pattern, which is typical of R1 (Mchaourab et al. [18] note that substitution to R3 which has one less sulfide bond, produced a single population of spins with isotropic motion).

## Conclusions

A molecular dynamics description of the spin probe and protein motions, such as the analysis presented in the

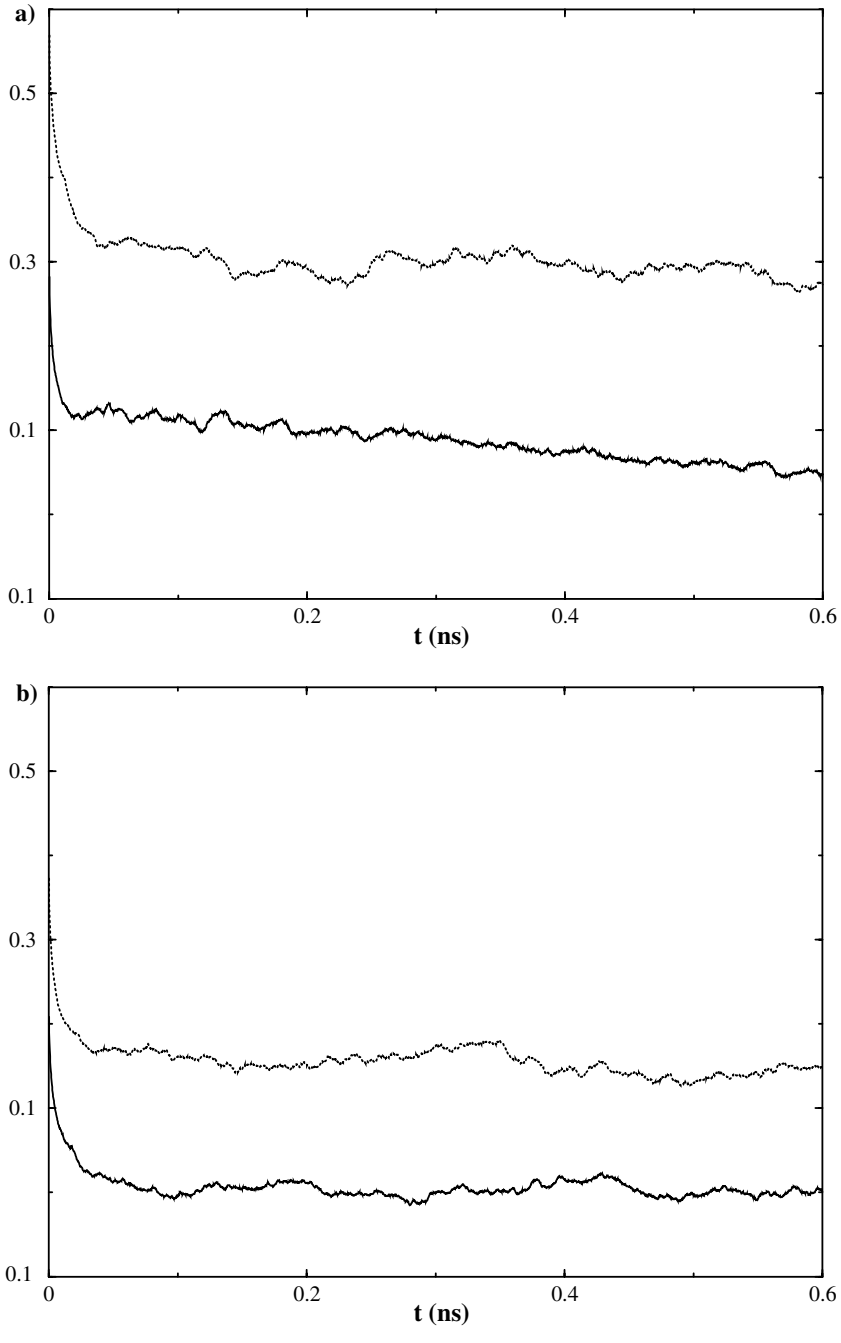


**Fig. 14** Torsion angle autocorrelation in mutant N40C: average over 8 3 ns-trajectories (**a** AMBER and **b** OPLS/AMBER); *solid line* $\chi_4$, *dotted line* $\chi_5$. *Left panel* the spin-probe R1 ring and the spin-probe Euler angles $\Omega$, $\theta$ and $\Phi$. *Middle panel* illustration of the "diffusion in a cone" model for the spin-probe motion: snapshots of helix B and of the R1 ring in N40C, taken at 0.3 ps intervals from AMBER trajectory 1, corrected for all-protein motion. *Right panel* the N40C mutant with the spin-label (*solid mode*), solvated in a *cubic box*

current work, offers the advantages of atomic detail and picosecond time resolution. In such simulations, restrictions in the rotational motions of the spin-label arise from forces between the spin-probe atoms and the neighboring protein residues, as well as solvent molecules. Thus, MD offers more realistic motional models, as compared to the traditional diffusion models with empirical parameters [8–11]. On the other hand, using atomically detailed MD trajectories to simulate EPR spectra poses a series of computational challenges, the most important of which is related to trajectory length [14, 17] and to the need for averaging over many initial conditions [17]. To these, the role of force field in spin probe (and protein) conformational sampling and equilibration should also be added. Different force fields may lead to differences in the sampling of spin-probe rotational and torsional degrees of freedom, which in fact define the contribution of the spin-probe classical molecular motions to the spin energies and ultemately to the EPR spectra. Different parametrizations of the interaction strengths between the spin probe and the protein backbone may have effects as important as complete motional narrowing of the spectra, and may thus obscure the more subtle site-dependent motional features.

In the present study, the analysis of local degrees of freedom in two T4L variants (N40C and K48C), and employing two different force fields (OPLS/AMBER and AMBER) led to the following conclusions:

In both mutants, the motion of the spin probe is essentially uncorrelated between one time step and the next, on the sub-picosecond time scale, supporting the use of Brownian diffusion as a model for spin-label motion [10–12]. Euler angle and torsion angle autocorrelation functions exhibit an inertial component (tens of picoseconds) and (at least) one diffusive component (hundreds of picoseconds to nanoseconds), corresponding to the spin-probe exploring high-probability regions in the space of rotational degrees of freedom, and to transitions between these states, respectively. More subtle differences in rotation rates about the spin ring axis in the two proteins could be detected from the AMBER trajectories, which were not apparent in the OPLS/AMBER analysis. In fact, the EPR spectra simulated from the OPLS/AMBER trajectories were found to be motionally averaged [17]. However, in many of the AMBER trajectories, equilibration in the rotation angle space was not achieved on the time scale of the simulation (3 ns), suggesting that longer time scales were needed in this case.

**Acknowledgements** The author wishes to acknowledge Dr. Ron Elber, Cornell University, for his support. This work was done during Ph.D. studies in the laboratory of Ron Elber. This research was supported by an NSF grant to RE.

## References

1. Freed JH (2000) Annu Rev Phys Chem 51:655–689
2. Borbat PP, Freed JH (1999) Chem Phys Lett 313:145–154
3. Borbat PP, Costa-Filho AJ, Earle KA, Moscicki JK, Freed JH (2001) Science 291:266–269
4. Columbus L, Hubbell WL (2002) Trends Biochem Sci 27:288–295
5. Columbus L, Kalai T, Jeko J, Hideg L, Hubbell WL (2002) Biochemistry 40:3828–3846
6. Ge M, Freed JH (1999) Biophys J 76:264–280
7. Schwartz LJ, Stillman AE, Freed JH (1982) J Chem Phys 77:5410–5425
8. Schneider DJ, Freed JH (1989) Calculating slow motional magnetic resonance spectra: a users guide. In: Berliner LJ, Reuben J (eds) Biological magnetic resonance, vol 8. Plenum Press NY, pp1–76
9. Fajer PG, Bennett RLH, Polnaszek CF, Fajer EA, Thomas DD (1990) J Magn Reson 88:111–125
10. Steinhoff HJ, Hubbell WL (1996) Biophys J 71:2201–2212
11. Robinson BH, Slutsky LJ, Auteri FP (1992) J Chem Phys 96:2609–2616
12. Usova N, Westlund PO, Fedchenia II (1995) J Chem Phys 103:96–103
13. Usova N, Perssoni L, Westlund PO (2000) Phys Chem Chem Phys 2:2785–2793
14. Hakansson P, Westlund PO, Lindahl E, Edholm O (2001) Phys Chem Chem Phys 3:5311–5319
15. LaConte LEW, Voelz V, Nelson W, Enz M, Thomas DD (2002) Biophys J 83:1854–1866
16. Levanon H, Mobius K (1997) Annu Rev Biophys Biomol Struct 26:495–540
17. Stoica I (2004) J Phys Chem B 108:1771–1782
18. Mchaourab HS, Lietzow MA, Hideg K, Hubbell WL (1999) Biochemistry 35:7692–7704
19. Stoica I (2004) J Biomol Struct Dyn 21:745–760
20. Mchaourab HS, Oh KJ, Fang CJ, Hubbell WL (1997) Biochemistry 36:307–316
21. Barnes J, Liang Z, Mchaourab H, Freed JH, Hubbell W (1999) Biophys J 76:3298–3306
22. Borbat PP, Mchaourab HS, Freed JH (2002) J Am Chem Soc 124:5304–5314
23. Spezia R, Aschi M, Di Nola A, Di Valentin M, Carbonera D, Amadei A (2003) Biophys J 84:2805–2813
24. MacKerell AD Jr, Wiorkiewicz-Kuczera J, Karplus M (1995) J Am Chem Soc 117:11946–11975
25. Elber R, Roitberg A, Simmerling C, Goldstein R, Li H, Verkhivker G, Keasar C, Zhang J, Ulitsky L (1995) Comp Phys Comm 91:159–189
26. Kaminski G, Friesner RA, Tirado-Rives J, Jorgensen WL (2001) J Phys Chem B 105:6474–6487
27. Arora K, Schlick T (2003) Chem Phys Lett 378:1–8
28. Andersen HC (1983) J Comput Phys 52:24–34
29. Darden TA, York DM, Pedersen LG (1993) J Chem Phys 98:10089–10092
30. Kabsch W (1976) Acta Cryst A 32:922–923
31. Kabsch W (1978) Acta Cryst A 34:827–828
32. Smith LJ, Daura X, van Gunsteren WF (2002) Proteins Struct Funct Genet 48:487–496
33. Jolicoeur C, Friedman HL (1971) Ber Bunsenges Phys Chem 75:248–257
34. Koradi R, Billeter M, Wüthrich K (1996) J Mol Graph 14:51–55